J Mol Model (2015) 21:46
DOI 10.1007/s00894-015-2590-8

ORIGINAL PAPER

A density functional theory study of hydrocarbon combustion and synthesis on Ni surfaces

Abas Mohsenzadeh · Tobias Richards · Kim Bolton

Received: 10 November 2014 / Accepted: 26 January 2015

Abstract Combustion and synthesis of hydrocarbons may occur directly (CH → C + H and CO → C + O) or via a formyl (CHO) intermediate. Density functional theory (DFT) calculations were performed to calculate the activation and reaction energies of these reactions on Ni(111), Ni(110), and Ni(100) surfaces. The results show that the energies are sensitive to the surface structure. The dissociation barrier for methylidyne (CH → C + H: catalytic hydrocarbon combustion) is lower than that for its oxidation reaction (CH + O → CHO) on the Ni(110) and Ni(100) surfaces. However the oxidation barrier is lower than that for dissociation on the Ni(111) surface. The dissociation barrier for methylidyne dissociation decreases in the order Ni(111) > Ni(100) > Ni(110). The barrier of formyl dissociation to CO and H is almost the same on the Ni(111) and Ni(110) surfaces and is lower compared to the Ni(100) surface. The energy barrier for carbon monoxide dissociation (CO → C + O: catalytic hydrocarbon synthesis) is higher than that of for its hydrogenation reaction (CO + H → CHO) on all three surfaces. This means that the hydrogenation to CHO is favored on these nickel surfaces. The energy barrier for both reactions decreases in the order Ni(111) > Ni(100) > Ni(110). The barrier for formyl dissociation to CH + O decreases in the order Ni(100) > Ni(111) > Ni(110). Based on these DFT calculations, the Ni(110) surface shows a better catalytic activity for hydrocarbon combustion compared to the other surfaces, and Ni is a better catalyst for the combustion reaction than for hydrocarbon synthesis, where the reaction rate constants are small. The reactions studied here support the BEP principles with R^2 values equal to 0.85 for C-H bond breaking/forming and 0.72 for C-O bond breaking /forming reactions.

Keywords DFT · Hydrocarbon combustion · Hydrocarbon synthesis · Nickel

Electronic supplementary material The online version of this article (doi:10.1007/s00894-015-2590-8) contains supplementary material, which is available to authorized users.

A. Mohsenzadeh (✉) · T. Richards · K. Bolton
Swedish Centre for Resource Recovery, University of Borås, SE 501-90 Borås, Sweden
e-mail: abas.mohsenzadeh@hb.se

T. Richards
e-mail: tobias.richards@hb.se

K. Bolton
e-mail: kim.bolton@hb.se

Introduction

The environmental consequences caused by fossil fuel combustion, such as production of pollutants and greenhouse gases, increases the importance of sustainable energy sources. Gasification is one of the most important and effective methods for sustainable energy generation. Generally, gasification means the conversion of carbonaceous material to a gaseous product, i.e., carbon monoxide and hydrogen (synthesis gas which is often referred to as syngas) with an employable heating value [1]. This gaseous product can further be converted into other hydrocarbons and liquid fuels that are combusted to H_2O and CO_2.

Catalytic combustion of hydrocarbons is an important technology, and has been developed for efficient energy production with minimum pollutant formation. It is done at lower temperatures compared to conventional flame combustion. The catalyst has played a decisive role in the improvement of this process [2–4]. Recent studies revealed that hydrocarbon oxidation is not a simple dissociation of the hydrocarbon

Published online: 18 February 2015

into hydrogen and carbon followed by oxidation reactions as assumed in previous studies [5, 6]. Instead, the direct reaction between CH fragments and oxygen can be the most important pathway. In this mechanism, an oxymethylidyne (CHO, formyl) intermediate is formed and subsequently dissociates to hydrogen and carbon monoxide [7, 8].

Since the early developmental work by Fischer and Tropsch and their co-workers [9], the synthesis of hydrocarbons from syngas is probably the most important source of chemicals and fuels from non-petroleum based sources. Fischer-Tropsch synthesis (FTS) is a complex catalytic process in which the synthesis gas is converted into various hydrocarbons and water over transition metals [10, 11]. The produced hydrocarbons can be utilized as feedstock in the chemical industry or as fuel. FTS has been investigated experimentally [12–14] and theoretically [8, 15, 16]. For the synthesis of hydrocarbons, a conclusion that was drawn from earlier studies was that both CO and H_2 are adsorbed on the catalyst surface and subsequently dissociate. Then both the C and O species are hydrogenated to CH_2 and H_2O [17]. However, recent investigations suggest that the reaction via CHO species is the main reaction pathway, similar to catalytic hydrocarbon combustion [18–21].

Inderwildi et al. [18] used DFT calculations and microkinetic simulations to study the FTS mechanism on a cobalt surface, and demonstrated that the main reaction pathway is the hydrogenation of CO (forming CHO) and subsequent cleavage of the C-O bond which yields co-adsorbed CH and O. They also investigated catalytic combustion and synthesis on noble metals [8], and found that the combustion and formation of hydrocarbons follow very similar routes but in opposite directions, and that CHO is an essential intermediate in both processes.

Zhu et al. [22] performed DFT calculations to investigate the methane reforming mechanism on the Ni(111) surface, which includes CHO formation and decomposition. They suggested that the oxidation step determines the overall reaction rate for both CH and C oxidation pathways. DFT calculations were used to study methanol decomposition on the Ni(111) and Ni(100) surfaces by Zhou et al. [23]. CHO formation and decomposition were also investigated in their study. They concluded that the methanol decomposition reaction mechanism may be sensitive to the surface structure. Wang et al. [24] investigated the reaction pathways of CO_2 reforming of CH_4 on the Ni(111) surface using DFT calculations. They found that CH oxygenation into CHO is more favored than its dissociation to C and H.

Goodman et al. [25] used Auger electron spectroscopy (AES) to investigate the kinetics of CO hydrogenation on the Ni(100) surface. Their results showed that a mechanism involving hydrogenation of an active carbon species was consistent with their kinetic data, and that the turnover number for methane formation is similar on the Ni(111) and Ni(100) surfaces. Hirano and Tanaka et al. [26, 27] used low energy electron diffraction (LEED) to study the methanation reaction of CO on Ni(111), Ni(110), and Ni(100) surfaces, and to explain why the catalytic activity of these surfaces does not appear to be sensitive to the surface structure. They found that the accumulation of overlayers of carbidic intermediates could be the reason. They concluded that the methanation reaction is catalyzed by the same compound that produces the carbide overlayers.

In contrast to methanation of CO on Ni surfaces, many studies indicate that the catalytic properties and reaction energies are affected by surface orientation, steps and defects [28–30]. Nickel particles grown on oxide or graphite substrates have polyhedral shapes exhibiting (111), (110), and (100) facets [31]. These facets have been investigated both theoretically and experimentally. As discussed above, investigations, e.g., of methanol decomposition, have been performed on the Ni(111) and Ni(100) surfaces, showing that they are stable under experimental conditions. The Ni(110) surface is also stable under experimental conditions. For example, Madix et al. [32] used high resolution electron energy loss vibrational spectroscopy to study the intermediate formed in the dehydration reaction for formic acid on Ni(110). They suggested that the lateral interactions between CO and HCOO cause the autocatalytic decomposition of the formate.

The present contribution provides a comparative DFT study of the combustion and the synthesis of hydrocarbons on the Ni(111), Ni(110), and Ni(100) surfaces. To the best of our knowledge this is the first time that the same methods and models are used for all surfaces and reactions to investigate how the reactant, transition state or product relative energies or vibrational frequencies are affected by the crystallographic structure of the nickel catalyst. These results are analyzed to identify which of the hydrocarbon combustion and synthesis reactions are kinetically favored on each of the surfaces, and whether these reactions follow the Brønsted-Evans-Polanyi (BEP) principles.

Methods and models

The calculations were performed using the Vienna ab initio simulation package (VASP) [33–36] implementing spin polarized DFT. The generalized gradient approximation with the Perdew, Burke, and Ernzerh of (GGA-PBE) formulation was used for the exchange-correlation functional [37]. The Kohn-Sham equations were solved using the projector-augmented wave method (PAW) [38, 39] with a 4×4×1 Monkhorst-Pack grid of k-points [40] for the numerical integration in reciprocal space. The Kohn-Sham orbitals were expanded in a plane-wave basis set using a kinetic energy cut off of 400 eV. Larger cut offs and finer k-meshes were also examined and yielded the same trends reported below. The conjugate-gradient (CG)

method was used for geometry optimization, and the minimum energy structure was identified when the change in the total energy and the forces acting on each ion became smaller than 10^{-5} eV and 10^{-3} eVÅ^{-1}, respectively.

A four-layer slab with a 2×2 unit cell was used to model the Ni surfaces. To provide a representative model of the semi-infinite bulk crystal, the two bottom layers of the slab were fixed and the two upper layers were free to relax. This slab size corresponds to a 1/4 and 1/2 monolayer coverage when there are one or two adsorbates, respectively, on the surface. This unit cell size yields converged results in a computationally feasible time and has been commonly used in investigations of similar systems [41–43]. Earlier studies have also shown that similar trends are obtained at lower surface coverages [44].

Transition states were found using the climbing image-nudged elastic band method [45, 46], where six images were placed between the reactant and product geometries. A – 5.0 eVÅ^{-2} spring force constant between images was used to relax the images until the maximum force acting on each ion was less than 0.1 eVÅ^{-1}. Calculations using a higher force convergence criterion of 0.01 eVÅ^{-1} changed the activation barrier by less than 0.2 meV. To confirm that the stationary structures were minimum energy (zero imaginary frequencies) or transition states (one imaginary frequency) and to calculate the vibrational partition functions and zero point vibrational energies (ZPVEs), vibrational frequency calculations were performed using ionic displacements of 0.01 Å. Only the adsorbates were allowed to move, and the frequencies were obtained by diagonalizing the finite difference Hessian matrix. This method has been successfully used in previous studies [47–49].

The adsorption energies (E_{ads}) of the reactants and products were calculated as $E_{ads} = E_{(surf+adsorbate)} - E_{surf} - E_{adsorbate}$ where $E_{surf+adsorbate}$ is the total energy of the surface-adsorbate(s) system, E_{surf} is the total energy of the surface and $E_{adsorbate}$ is the total energy of the isolated, geometry optimized adsorbate(s) in vacuum. The rate constants (k) were estimated from transition state theory [50] using Eq. 1:

$$k = \left(\frac{k_B T}{h}\right)\left(\frac{q^{\ddagger}}{q}\right) e^{\frac{-E_a}{k_B T}}, \quad (1)$$

where k_B is Boltzmann's constant, T is the absolute temperature, and h is Planck's constant. q and $q^{\ddagger}$ are the partition functions for the reactant and the transition state, respectively, and E_a is the ZPVE corrected activation energy. The partition functions were calculated using harmonic vibrations. Although this approximation may affect the quantitative results presented here, it is not expected to affect the trends [29, 47, 51].

The different surface sites that are present on the Ni(111), Ni(110), and Ni(100) surfaces and that were investigated are shown in Fig. 1.

The first principles data were used to model the kinetics of the hydrocarbon synthesis reaction via the direct dissociation route (CO ⇌ C+O followed by C + H → CH) and the formyl route (CO +H ⇌ CHO followed by CHO → CH + O). The ODE23s solver in the MATLAB R2013a simulation package [52] was employed to solve the ordinary differential equations for the mechanisms discussed below.

Results and discussion

Geometry optimizations were performed for all adsorption sites shown in Fig. 1 and for different orientations of the adsorbates. The lowest energy structures, where a transition state was found between reactants and products, were then selected for further investigation of the reaction mechanisms and rates. Details of the transition states, adsorption, and co-adsorption energies for the most stable configurations, together with the

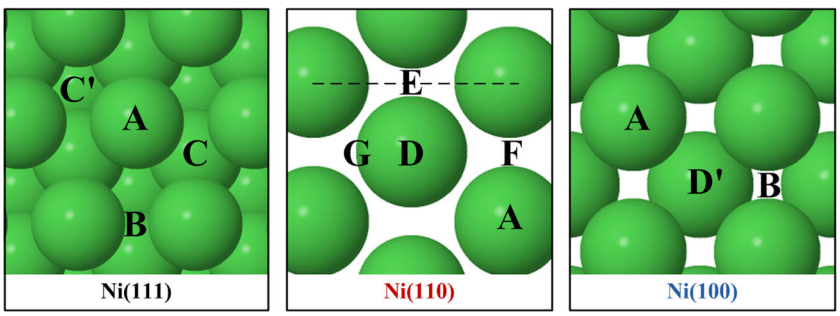

Fig. 1 Different adsorption sites on the Ni(111), Ni(110), and Ni(100) surfaces. A is a top site; B is a bridge site; C is a hcp site; C′ is a fcc site; D is a rectangular fourfold hollow site; D′ is a square fourfold hollow site; E is a long bridge site; F is a short bridge site; G is a pseudo 3-fold hollow site. The color coding for Ni(111) (black), Ni(110) (red), and Ni(100) (blue) surfaces are used throughout this contribution. The Ni atoms are shown in green

structural parameters, are given in Tables S1-S4 in the Supporting information.

Catalytic hydrocarbon combustion

The activation and reaction energies as well as the reaction rate constants calculated at 600 K, which is a typical temperature for synthesis and low temperature catalytic combustion of hydrocarbons [53–55], are given in Table 1 together with results of previous studies when available.

The calculated activation energies for dissociation of CH are 1.15 eV, 0.33 eV, and 0.45 eV on the Ni(111), Ni(110), and Ni(100) surfaces, respectively. The reaction energies are 0.49 eV on the Ni(111) surface, −0.22 eV on the Ni(110) surface and –0.21 eV on the Ni(100) surface. Hence, the reaction is exothermic on the Ni(110) and Ni(100) surfaces while it is endothermic on the Ni(111) surface.

In contrast to dissociation, the lowest activation energy for CH oxidation was obtained on the Ni(111) surface, i.e., 0.85 eV compared to 1.43 eV and 2.46 eV on the Ni(110) and Ni(100) surfaces. The oxidation reaction is exothermic on the Ni(111) surface while it is endothermic on the other surfaces.

The effect of the surface structure on the height of the activation barrier for formyl dissociation to CO and H follows the same order as methylidyne oxidation, and the reaction is exothermic on all surfaces. The activation barriers are 0.15 eV, 0.16 eV, and 0.48 eV for the Ni(111), Ni(110), and Ni(100) surfaces, respectively.

The trends in the relative activation and reaction energies obtained for the Ni(111) and Ni(100) surfaces are similar to those reported previously. Li et al. [57] found a lower barrier for CH dissociation on the Ni(100) surface, i.e., 0.64 eV, compared to 1.38 eV on the Ni(111) surface. Blaylock et al. [58] also found similar trends, i.e., 0.91 eV, on the Ni(100) surface compared to 1.40 eV on the Ni(111) surface. The trends of the reaction energies reported in the previous studies are also similar to what is obtained in this work, i.e., the reaction on the Ni(111) surface is endothermic while the reaction on Ni(100) surface is exothermic. It also should be noted that the reaction energy obtained by Wang et al. [24], 1.21 eV, is larger compared to what is reported here since they found different co-adsorption sites for C and H. They reported a reaction energy of 0.59 eV for the sum of separated adsorbed species.

Blaylock et al. [58] reported a higher CH oxidation activation energy on the Ni(100) surface, i.e., 2.02 eV, compared to 1.36 eV on the Ni(111) surface and the reaction on both surfaces are endothermic. However, Wang et al. [24] found an exothermic reaction on the Ni(111) surface similar to the present work. The reason for the difference is not clear but it may be due to different adsorption sites investigated. Similar to our results, Zhou et al. [23] obtained a lower CHO to CO and H dissociation barrier on the Ni(111) surface compare to the

Table 1 The activation energies (eV), reaction rate constants at 600 K (s^{-1}) and reaction energies (eV) involved in the hydrocarbon combustion reaction[a]

Catalytic hydrocarbon combustion										
	CH → C + H			CH + O → CHO			CHO → CO + H			
	E_a	k	ΔE	E_a	k	ΔE	E_a	k	ΔE	
Ni(111)	1.15	2.47×10^{3}	0.49	0.85	1.14×10^{6}	− 0.30	0.15	4.17×10^{11}	− 1.38	
Previous results	1.32[b], 1.37[c], 1.33[e], 1.38[f], 1.40[g]		1.21[c], 0.42[f], 0.55[g]	1.43[b], 0.80[c], 1.53[e], 1.36[g]		− 0.51[c], 0.32[g]	0.20[b], 0.29[c], 0.18[d], 0.20[e]		− 1.18[c], − 1.34[d], − 1.35[g]	
Ni(110)	0.33	5.90×10^{9}	− 0.22	1.43	1.01×10^{1}	0.54	0.16	6.79×10^{11}	− 1.13	
Previous results										
Ni(100)	0.45	1.35×10^{9}	− 0.21	2.46	3.59×10^{-8}	0.59	0.48	7.94×10^{9}	− 0.88	
Previous results	0.64[f], 0.91[g]		− 0.03[f], − 0.23[g]	2.02[g]		0.75[g]	0.79[d]		− 0.57[d], − 0.80[g]	

[a] The activation and reaction energies are ZPVE-corrected values. [b] Ref [56] (GGA-PW91 calculations using a 2×2 unit cell and four layer slab). [c] Ref [24] (GGA-PBE calculations using a 2×2 unit cell and three layer slab). [d] Ref [23] (GGA-PBE calculations using a 3×2 unit cell and three layer slab). [e] Ref [22] (GGA-PW91 calculations using a 3×3 unit cell and four layer slab). [f] Ref [57] (GGA-RPBE calculations using a 2×2 unit cell and four layer slab). [g] Ref [58] (GGA-RPBE calculations using a 3×3 unit cell and four layer slab)

Ni(100) surface, i.e. 0.18 eV and 0.79 eV, respectively, where both reaction are exothermic.

No results have previously been reported for the Ni(110) surface. The trends observed here (e.g., the effect of the surface structure on the barrier height and reaction energies), as well as those in the "Catalytic hydrocarbon synthesis" section, are discussed in the "Brønsted-Evans-Polanyi principle and reaction profiles" section.

The geometries of the reactants, transition states and products which are presented in Table 1, are shown in Fig. 2. The adsorption and co-adsorption energies, together with the details of these structures, are given in Tables S1, S3, and S4 in the Supporting information.

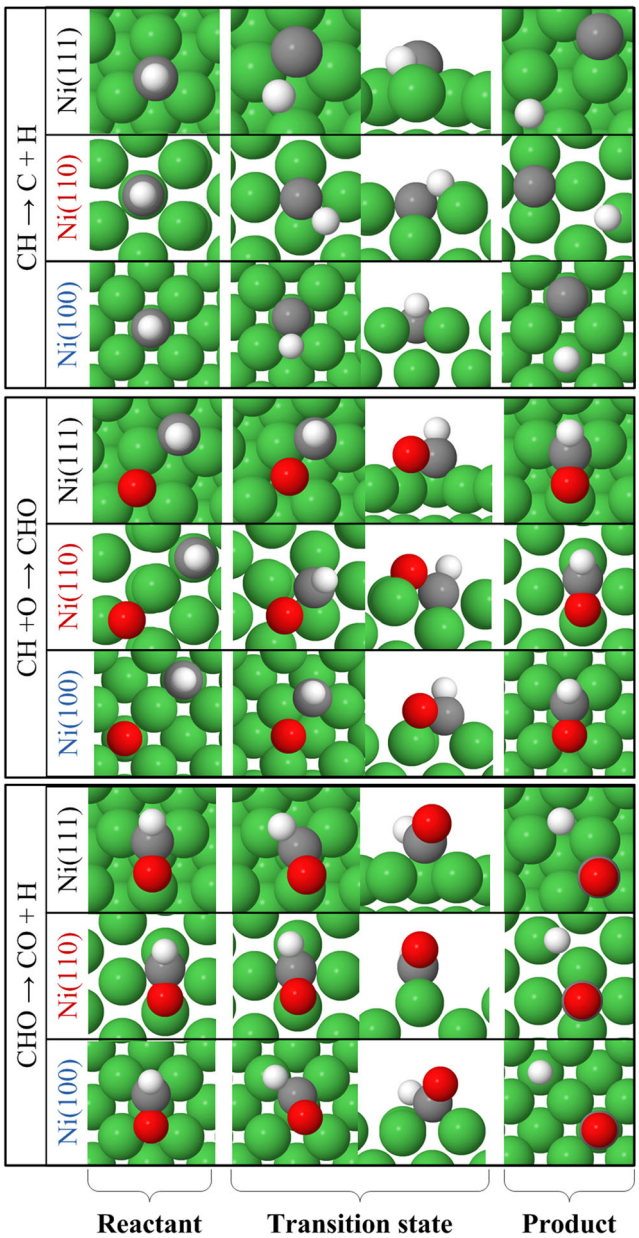

Fig. 2 Reactant, transition state, and product structures for the reactions involved in catalytic hydrocarbon combustion. Color coding is the same as in Fig. 1. In addition, oxygen atoms are shown in red, carbon in gray, and hydrogen in white

Catalytic hydrocarbon synthesis

The activation barriers, rate constants at 600 K and reaction energies for hydrocarbon synthesis are given in Table 2.

The highest activation energy for CO dissociation is on the Ni(111) surface, and is 2.99 eV compared to 1.98 eV and 1.83 eV on the Ni(100) and Ni(110) surfaces, respectively. The reaction is endothermic on all three surfaces.

The activation energy for the hydrogenation of CO follows the same order as its dissociation, i.e., it decreases in the order of Ni(111) > Ni(100) > Ni(110). The reaction is endothermic on all surfaces with reaction energies of 1.38 eV, 1.13 eV and 0.88 eV for the Ni(111), Ni(110) and Ni(100) surfaces, respectively.

The barrier of formyl dissociation to CH and O, however, decreases in the order of Ni(100) > Ni(111) > Ni(110). The reaction on the Ni(110) and Ni(100) surfaces is exothermic while it is endothermic on the Ni(111) surface.

The results obtained in the present study are similar to those reported previously (which are shown in Table 2 and are only available for the Ni(111) surface).

Figure 3 shows geometries of the reactants, transition states and products for the reactions given in Table 2. The adsorption and co-adsorption energies together with the details of these structures are given in Tables S2, S3, and S4 in the Supporting information.

Brønsted-Evans-Polanyi principle and reaction profiles

According to the Brønsted-Evans-Polanyi (BEP) principle the activation energy for a given reaction should be linearly proportional to the reaction energy [59, 60]. Figure 4 shows these correlations for the different Ni surface structures studied here (the data used to draw Fig. 4 is provided in Table S5 in the Supporting information). Results from C-H bond breaking/forming are combined in the upper panel and those for C-O bond breaking/forming are shown in the lower panel.

Figure 4 reveals that these reactions support the BEP principle with R^2 values of 0.85 and 0.72 for C-H and C-O bond breaking/forming and, respectively. However, it should be noted that only three Ni facets have been studied in this work and more facets would improve the statistical relevance of the results.

Including all of the data in a single plot, as done in Fig. S1 (a) in the Supporting information, yields an R^2=0.53. This deterioration of the fit to the BEP principle is expected since the chemical species involved in these groups of reactions and also the reactivity of the surfaces are different [61].

The transition state scaling (TSS) method [61, 62], which is related to the BEP principle, correlates the transition state

Table 2 The activation energies (eV), reaction rate constants at 600 K (s^{-1}), and reaction energies (eV) for the reactions involved in hydrocarbon synthesis[a]

	Catalytic hydrocarbon synthesis								
	CO → C + O			CO + H → CHO			CHO → CH + O		
	E_a	k	ΔE	E_a	k	ΔE	E_a	k	ΔE
Ni(111)	2.99	8.20×10^{-14}	2.60	1.53	1.22×10^{0}	1.38	1.16	5.28×10^{2}	0.30
Previous results	3.01[b], 2.94[c], 3.15[d]		2.51[d]	1.35[b], 1.48[c], 1.47[d]		1.18[d]	1.28[b], 1.08[c], 1.31[d]		0.51[d]
Ni(110)	1.83	2.94×10^{-4}	0.76	1.29	1.00×10^{2}	1.13	0.89	6.39×10^{4}	– 0.54
Previous results									
Ni(100)	1.98	1.94×10^{-5}	0.82	1.36	3.83×10^{1}	0.88	1.86	2.55×10^{-3}	– 0.59
Previous results									

[a] The activation and reaction energies are ZPVE-corrected values. [b] Ref [56] (GGA-PW91 calculations using a 2×2 unit cell and four layer slab). [c] Ref [22] (GGA-PW91 calculations using a 3×3 unit cell and four layer slab). [d] Ref [24] (GGA-PBE calculations using a 2×2 unit cell and three layer slab)

energy (E_{TS}) with either the initial state (E_{IS}) or final state (E_{FS}) energy (i.e., the energy of the reactants or products). In the present work correlation with the initial state is the same as with the final state since both the forward (bond breaking) and backward (bond forming) reactions are included in the plots. Similar to previous studies [56, 63], correlation between E_{TS} and E_{FS} (shown in Fig. S1 (b) in the Supporting information) yields a larger R^2 (0.96) than that obtained in the BEP plot (0.53). This is partly due to the larger energy intervals in the TSS plot compared to the BEP plot [64].

Figure 5 shows the reaction profiles for hydrocarbon combustion. The calculations reveal that, when there is sufficient co-adsorbed oxygen on the Ni(111) surface, the fraction of CH that undergoes direct dissociation prior to oxidation is very small due to its higher activation barrier (1.15 eV compared to 0.85 eV). The same trends were also observed by Wang et al. [24]. They found a dissociation barrier of 1.37 eV and an oxidation barrier of 0.80 eV on the Ni(111) surface.

In contrast, the dissociation barrier on the Ni(110) and Ni(100) surfaces is lower than the oxidation barriers. These trends are similar to what was reported by Blaylock et al. [58]. They found that the oxidation and dissociation barriers follow opposite orders on the Ni(111) and Ni(100) surfaces, i.e., on the Ni(111) surface the dissociation has a higher activation energy compared to oxidation while on the Ni(100) surface the dissociation has a lower energy barrier compared to oxidation. It is also apparent from Fig. 5 that if the Ni(110) and/or Ni(100) surfaces are present with a sufficiently large area, direct combustion of CH to C and H is preferred to oxidation via a CHO intermediate. That is, the lowest activation energy for the formation of the CHO intermediate is 0.85 eV (on the Ni(111) surface) which is larger than the lowest barriers for direct combustion (on the Ni(110) and Ni(100) surfaces).

Experimental investigations also support the lower barrier obtained for carbon formation on the Ni(110) surface compared to the Ni(111) surface. Atoms in the Ni(110) surface ridges have lower coordination numbers, which is the same for atoms in the stepped Ni(211) surface, and Abild-Pedersen et al. [65] reported that carbon formation is preferred on the stepped Ni(211) surface compared to the Ni(111) surface.

The d-band center, which describes the distribution of surface electronic energy levels [57, 66] and demonstrates the ability to eject an electron from the d-band of the metal to the adsorbate, can be used to explain differences in catalytic activity of the different surfaces. The calculated d-band centers are at –1.75, −1.98 and –2.08 eV for the Ni(110), Ni(100), and Ni(111) surfaces, respectively [30]. Generally, the surface is more reactive when the d-band center is closer to the Fermi level [57, 66]. Thus, the Ni(110) surface is expected to be the most reactive surface and the activity of different surfaces decreases in the order Ni(110) > Ni(100) > Ni(111). For catalytic hydrocarbon combustion, the reaction rate constants (k values given in Table 1) for CH and CHO dissociation are largest on the Ni(110) surface as expected. However, the rate constant for CH oxidation is bigger on the Ni(111) surface compared to the other surfaces.

The reaction profiles for hydrocarbon synthesis are compared in Fig. 6. Except for CHO dissociation to CH and O, where the barrier on the Ni(100) surface is higher compared to the Ni(111) surface, the activation energies on the different surfaces increases in the order Ni(110) < Ni(100) < Ni(111). This trend is also expected from the positions of the d-band centers discussed above. It is evident that the activation energies for CO dissociation are higher on all surfaces compared to its hydrogenation. It may also be noted that the adsorption energies of CO are –1.89 eV, −1.89 eV, and –1.96 eV on the Ni(111), Ni(110), and Ni(100), respectively (see Table S2). Therefore, CO desorption will compete with dissociation on the Ni(111) and Ni(100) surfaces, while CO dissociation is favored on the Ni(110) surface.

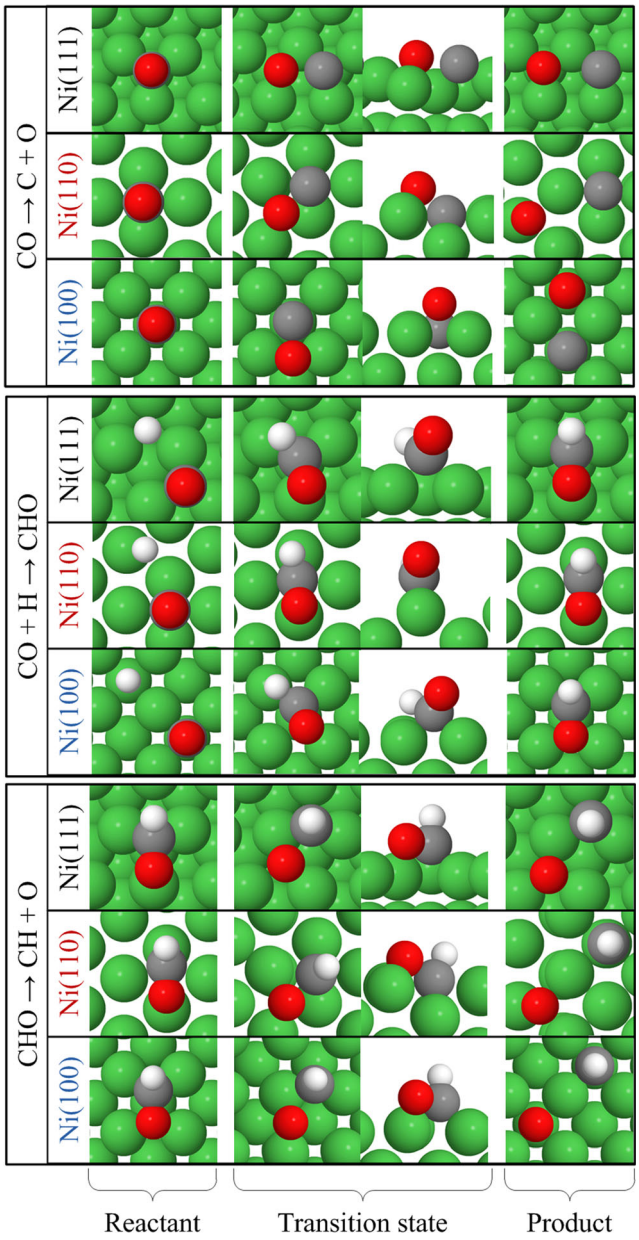

Fig. 3 Reactant, transition state, and product structures for the reactions involved in catalytic hydrocarbon synthesis. Color coding is the same as in Fig. 2

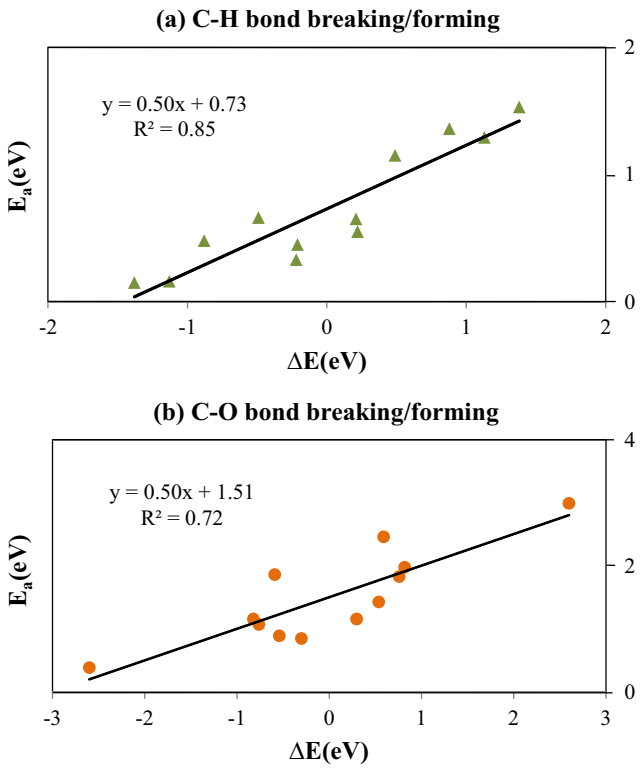

Fig. 4 Brønsted-Evans-Polanyi (BEP) correlations for (a) C-H and (b) C-O bond breaking/forming reactions on the Ni(111), Ni(110) and Ni(100) surfaces

When hydrogen is co-adsorbed on the Ni surface the CO can react with these atoms instead of dissociating to C + O or desorbing. In this case, CO + H forms CHO. In fact, the activation energies for CHO formation are lower than those for CO dissociation and desorption on all surfaces. The adsorbed CO species is therefore more likely to react with co-adsorbed hydrogen than to dissociate to C and O or to desorb from the surface. These findings are in agreement with the results of temperature programmed desorption experiments done by Andersson et al. [19] in which no CO dissociation was observed on the CO-covered Ni(111) surface. They suggested that the reaction via a formyl species has a barrier below the desorption energy. The preferred formation of CHO could also be the reason why the formation of volatile carbonyls are observed for the Fischer-Tropsch process on Ni [67, 68].

Figure 7 shows the time dependence of the CH concentration produced via the direct dissociation route (CO ⇌ C+O followed by C + H → CH) and the formyl route (CO +H ⇌ CHO followed by CHO → CH + O) on the three different Ni surfaces. The temperature is 600 K. The data in the Supporting information shows that the desorption energies of the species involved in these reactions are larger than the barriers shown in Figs. 5 and 6. Hence, at moderate pressures all species will be present on the metal surface. Figure 6 shows the average rate of CH formation from each CO molecule on the surface (therefore the concentration of the produced CH increases until it reaches 1). It is evident that both routes are fastest on the Ni(110) surface. Also, the direct route is faster on the Ni(110) and Ni(100) surfaces compared to the formyl route. However, the formyl route will dominate if the Ni(111) surface is used. Similar trends were observed when different H concentrations (between 0.25 and 1.5) were used in the kinetics model.

Since the rate constants (see Table 2) for synthesis reactions are far smaller than those for the combustion reactions (see

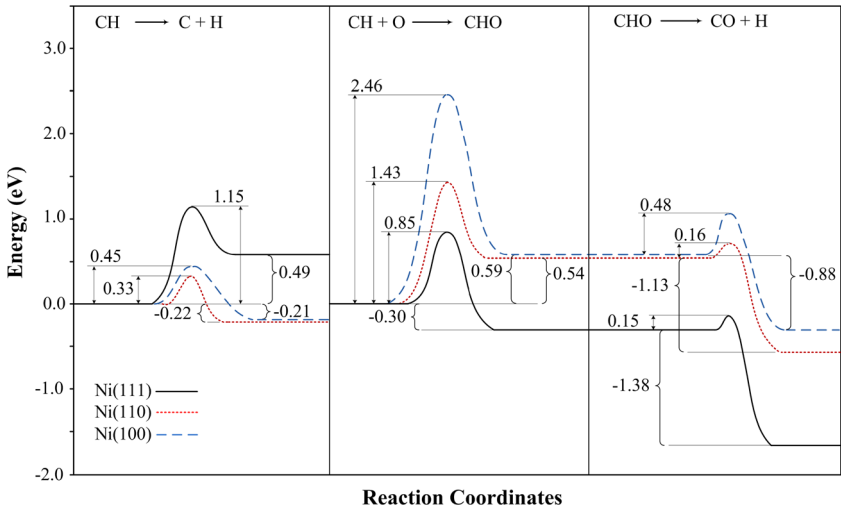

Fig. 5 Reaction profiles for catalytic hydrocarbon combustion. Color coding is the same as in Fig. 1

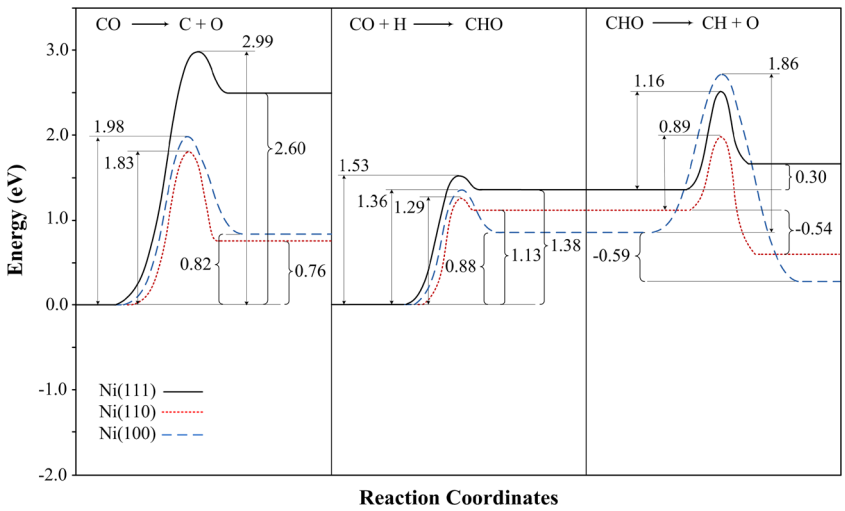

Fig. 6 Reaction profiles for catalytic hydrocarbon synthesis. Color coding is the same as in Fig. 1

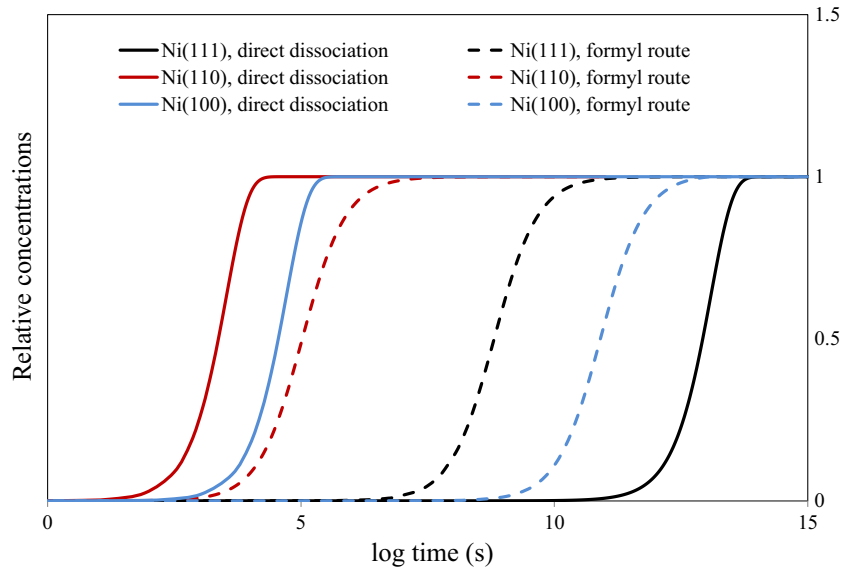

Fig. 7 Time dependence of the relative concentration of CH produced on Ni(111), Ni(110), and Ni(100) surfaces via direct dissociation (solid lines) and via formyl intermediate (dashed lines). The temperature is 600 K and the initial concentration of adsorbed CO and H are 1 (arbitrary units of concentration). Color coding is the same as in Fig. 1

Table 1), Ni is a better catalyst for hydrocarbon combustion. This could be the reason for the insensitivity of catalytic activity to the surface structure that has been observed experimentally for FTS reactions [25–27]. It may also be noted that although the transition state theory is expected to be valid when the activation energy is large (since the slow reaction rate will allow for equilibration of vibrational energy in the reactant(s)), it may not be as good as an approximation for some of the faster reactions, such as CHO → CH+O on the Ni(111) and Ni(110) surfaces.

Conclusions

The effect of three common nickel surface structures on the reaction energetics of hydrocarbon combustion and synthesis has been systematically examined by DFT calculations using the same models and methods. The results show that the reaction barriers are sensitive to the surface structure. For catalytic hydrocarbon combustion, the CH dissociation barrier is lower compared to its oxidation activation energy on the Ni(110) and Ni(100) surfaces. In contrast, the dissociation barrier is higher on the Ni(111) surface. This means that dissociation is favored on the Ni(110) and Ni(100) surfaces, while oxidation to CHO is favored on the Ni(111) surface. The dissociation barrier increases in the order Ni(110) < Ni(100) < Ni(111) and the oxidation barrier decreases in the order Ni(100) > Ni(110) > Ni(111). The barrier for CHO dissociation to CO and H follows the same order as CH oxidation.

For the catalytic hydrocarbon synthesis, the CO dissociation barrier is significantly higher compared to its hydrogenation barrier on all surfaces, which means that hydrogenation to CHO is favored over nickel in the presence of sufficient coadsorbed H. This could explain why formation of carbonyls in the nickel-catalyzed Fischer-Tropsch process is observed experimentally [67, 68]. The rate of both reactions decreases in the order Ni(110) > Ni(100) > Ni(111). For the formyl dissociation to CH and O, the lowest barrier was obtained on the Ni(110) surface. The barrier on the Ni(100) surface is higher compared to the Ni(111) surface, unlike the oxidation and hydrogenation reactions. Also, the barrier for CHO dissociation to CH and O is higher than the dissociation to CO and H. The calculated rate constants at 600 K are rather small for the synthesis process, which could be a reason for the experimental observations that the Fischer-Tropsch process is insensitive to the Ni surface orientation.

Hence, based on DFT calculations, the Ni(110) surface showed a better catalytic activity for hydrocarbon combustion than for hydrocarbon synthesis.

The reactions studied support the BEP relations with R^2 values of 0.85 for C-H bond breaking/forming and 0.85 for C-O bond breaking/forming. Also the d-band center provides a valid description for the relative catalytic activity of all facets of the Ni surface, except for CH oxidation which is faster on the Ni(111) surface even though the d-band center for this facet is farthest from the Fermi level.

Acknowledgments This research is funded by Stiftelsen Föreningssparbanken Sjuhärad. The computations and simulations were performed on resources provided by the Swedish National Infrastructure for Computing (SNIC) at PDC Centre for High Performance Computing (PDC-HPC) and the Uppsala Multidisciplinary Centre for Advanced Computational Science (UPPMAX). We also acknowledge that the results of this research have been achieved using the PRACE-2IP project (FP7 RI-283493) resource Abel based in Norway at UiO.

References

1. Higman C, Burgt M (2008) Gasification, 2nd edn. Gulf Professional, Oxfrod
2. Yazawa Y, Takagi N, Yoshida H, Komai S-i, Satsuma A, Tanaka T, Yoshida S, Hattori T (2002) The support effect on propane combustion over platinum catalyst: control of the oxidation-resistance of platinum by the acid strength of support materials. Appl Catal A 233(1–2):103–112
3. Anderson RB, Stein KC, Feenan JJ, Hofer LJE (1961) Catalytic oxidation of methane. Ind Eng Chem Res 53(10):809–812
4. Skoglundh M, Fridell E (2004) Strategies for enhancing low-temperature activity. Top Catal 28(1–4):79–87
5. Bizzi M, Saracco G, Schwiedernoch R, Deutschmann O (2004) Modeling the partial oxidation of methane in a fixed bed with detailed chemistry. AIChE J 50(6):1289–1299
6. Horn R, Williams KA, Degenstein NJ, Schmidt LD (2006) Syngas by catalytic partial oxidation of methane on rhodium: mechanistic conclusions from spatially resolved measurements and numerical simulations. J Catal 242(1):92–102. doi:10.1016/j.jcat.2006.05.008
7. Inderwildi OR, Jenkins SJ, King DA (2007) An unexpected pathway for the catalytic oxidation of methylidyne on Rh{111} as a route to syngas. J Am Chem Soc 129(6):1751–1759
8. Inderwildi OR, Jenkins SJ, King DA (2008) Mechanistic studies of hydrocarbon combustion and synthesis on noble metals. Angew Chem Int Ed 47(28):5253–5255
9. Fischer F, Tropsch H (1923) The preparation of synthetic oil mixtures (synthol) from carbon monoxide and hydrogen. Brennst Chem 4: 276–285
10. Dry ME (1996) Practical and theoretical aspects of the catalytic Fischer-Tropsch process. Appl Catal A 138(2):319–344
11. Schulz H (1999) Short history and present trends of Fischer-Tropsch synthesis. Appl Catal A 186(1–2):3–12
12. Brady RC, Pettit R (1980) Reactions of diazomethane on transition-metal surfaces and their relationship to the mechanism of the Fischer-Tropsch reaction. J Am Chem Soc 102(19):6181–6182
13. Brady RC, Pettit R (1981) Mechanism of the Fischer-Tropsch reaction. The chain propagation step. J Am Chem Soc 103(5):1287–1289
14. Wilson J, de Groot C (1995) Atomic-scale restructuring in high-pressure catalysis. J Phys Chem Us 99(20):7860–7866
15. Liu Z-P, Hu P (2002) A new insight into Fischer−Tropsch synthesis. J Am Chem Soc 124(39):11568–11569
16. Ciobîcă IM, Kramer GJ, Ge Q, Neurock M, van Santen RA (2002) Mechanisms for chain growth in Fischer–Tropsch synthesis over Ru(0001). J Catal 212(2):136–144

17. Klinke Ii DJ, Broadbelt LJ (1999) Construction of a mechanistic model of Fischer–Tropsch synthesis on Ni(111) and Co(0001) surfaces. Chem Eng Sci 54(15–16):3379–3389
18. Inderwildi OR, Jenkins SJ, King DA (2008) Fischer-Tropsch mechanism revisited: alternative pathways for the production of higher hydrocarbons from synthesis gas. J Phys Chem C 112(5):1305–1307
19. Andersson MP, Abild-Pedersen F, Remediakis IN, Bligaard T, Jones G, Engbæk J, Lytken O, Horch S, Nielsen JH, Sehested J, Rostrup-Nielsen JR, Nørskov JK, Chorkendorff I (2008) Structure sensitivity of the methanation reaction: H_2-induced CO dissociation on nickel surfaces. J Catal 255(1):6–19
20. Coenen JWE, van Nisselrooy PFMT, de Croon MHJM, van Dooren PFHA, van Meerten RZC (1986) The dynamics of methanation of carbon monoxide on nickel catalysts. Appl Catal 25(C):1–8
21. Andersson MP, Bligaard T, Kustov A, Larsen KE, Greeley J, Johannessen T, Christensen CH, Nørskov JK (2006) Toward computational screening in heterogeneous catalysis: Pareto-optimal methanation catalysts. J Catal 239(2):501–506
22. Zhu Y-A, Chen D, Zhou X-G, Yuan W-K (2009) DFT studies of dry reforming of methane on Ni catalyst. Catal Today 148(3–4):260–267
23. Zhou Y-H, Lv P-H, Wang G-C (2006) DFT studies of methanol decomposition on Ni(100) surface: compared with Ni(111) surface. J Mol Catal A Chem 258(1):203–215
24. Wang S-G, Liao X-Y, Hu J, Cao D-B, Li Y-W, Wang J, Jiao H (2007) Kinetic aspect of CO_2 reforming of CH_4 on Ni(111): a density functional theory calculation. Surf Sci 601(5):1271–1284
25. Goodman DW, Kelley RD, Madey TE, Yates JT Jr (1980) Kinetics of the hydrogenation of CO over a single crystal nickel catalyst. J Catal 63(1):226–234
26. Hirano H, Tanaka K (1993) Structure and reactivity of carbidic intermediates for the methanation reaction on Ni(100), Ni(111), and Ni(110) surfaces. Stud Surf Sci Catal 75:1575–1578
27. Hirano H, Tanaka K (1992) A reason for the structure-insensitive catalytic activity of Ni(100) and Ni(111) surfaces for the methanation reaction of CO. J Catal 133(2):461–466
28. Nørskov JK, Bligaard T, Hvolbæk B, Abild-Pedersen F, Chorkendorff I, Christensen CH (2008) The nature of the active site in heterogeneous metal catalysis. Chem Soc Rev 37(10):2163–2171
29. Fajín JL, Cordeiro M, Illas F, Gomes JR (2009) Influence of step sites in the molecular mechanism of the water gas shift reaction catalyzed by copper. J Catal 268(1):131–141
30. Mohsenzadeh A, Bolton K, Richards T (2014) DFT study of the adsorption and dissociation of water on Ni(111), Ni(110) and Ni(100) surfaces. Surf Sci
31. Henry CR (1998) Surface studies of supported model catalysts. Surf Sci Rep 31(7):231–325
32. Madix RJ, Gland JL, Mitchell GE, Sexton BA (1983) Identification of the intermediates in the dehydration of formic acid on Ni(110) by high resolution electron energy loss vibrational spectroscopy. Surf Sci 125(2):481–489
33. Kresse G, Hafner J (1993) Ab initio molecular dynamics for liquid metals. Phys Rev B 47(1):558
34. Kresse G, Hafner J (1994) Ab initio molecular-dynamics simulation of the liquid-metal–amorphous-semiconductor transition in germanium. Phys Rev B 49(20):14251
35. Kresse G, Furthmüller J (1996) Efficiency of ab-initio total energy calculations for metals and semiconductors using a plane-wave basis set. Comput Mater Sci 6(1):15–50
36. Kresse G, Furthmüller J (1996) Efficient iterative schemes for ab initio total-energy calculations using a plane-wave basis set. Phys Rev B 54(16):11169
37. Perdew JP, Burke K, Ernzerhof M (1996) Generalized gradient approximation made simple. Phys Rev Lett 77(18):3865
38. Pan Y, Zhang H, Shi D, Sun J, Du S, Liu F, Gao H (2009) Highly ordered, millimeter-scale, continuous, single-crystalline graphene monolayer formed on Ru (0001). Adv Mater 21(27):2777–2780
39. Blöchl PE (1994) Projector augmented-wave method. Phys Rev B 50(24):17953
40. Monkhorst HJ, Pack JD (1976) Special points for Brillouin-zone integrations. Phys Rev B 13(12):5188–5192
41. Wang S-G, Cao D-B, Li Y-W, Wang J, Jiao H (2005) Chemisorption of CO_2 on nickel surfaces. J Phys Chem B 109(40):18956–18963
42. Ciobica I, Frechard F, Van Santen R, Kleyn A, Hafner J (2000) A DFT study of transition states for CH activation on the Ru (0001) surface. J Phys Chem B 104(14):3364–3369
43. Ledentu V, Dong W, Sautet P (2000) Heterogeneous catalysis through subsurface sites. J Am Chem Soc 122(8):1796–1801
44. Mohsenzadeh A, Borjesson A, Wang J-H, Richards T, Bolton K (2013) The effect of carbon monoxide co-adsorption on Ni-catalysed water dissociation. Int J Mol Sci 14(12):23301–23314
45. Henkelman G, Uberuaga BP, Jónsson H (2000) A climbing image nudged elastic band method for finding saddle points and minimum energy paths. J Chem Phys 113:9901
46. Henkelman G, Jónsson H (2000) Improved tangent estimate in the nudged elastic band method for finding minimum energy paths and saddle points. J Chem Phys 113:9978
47. Fajín JL, Cordeiro M, Illas F, Gomes JR (2010) Descriptors controlling the catalytic activity of metallic surfaces toward water splitting. J Catal 276(1):92–100
48. Fajín JL, Cordeiro M, Illas F, Gomes JR (2014) Generalized Brønsted–Evans–Polanyi relationships and descriptors for O–H bond cleavage of organic molecules on transition metal surfaces. J Catal 313:24–33
49. Shojaee K, Montoya A, Haynes BS (2013) Insight into oxygen stability and vacancy formation on Co3O4 model slabs. Comput Mater Sci 72:15–25
50. Chorkendorff I, Niemantsverdriet JW (2006) Concepts of modern catalysis and kinetics. Wiley, Weinheim
51. van Harrevelt R, Honkala K, Nørskov JK, Manthe U (2005) The reaction rate for dissociative adsorption of N on stepped Ru (0001): Six-dimensional quantum calculations. J Chem Phys 122:234702
52. MATLAB R2014a (2013) The Mathworks Inc, Natick
53. Enger BC, Holmen A (2012) Nickel and Fischer-Tropsch synthesis. Cat Rev 54(4):437–488
54. Li N, Gaillard F, Boréave A (2008) Electrochemical promotion of Ag catalyst for the low temperature combustion of toluene. Catal Commun 9(6):1439–1442
55. Wu M, Wang X, Dai Q, Gu Y, Li D (2010) Low temperature catalytic combustion of chlorobenzene over Mn–Ce–O/γ-Al2O3 mixed oxides catalyst. Catal Today 158(3–4):336–342
56. Catapan RC, Oliveira AA, Chen Y, Vlachos DG (2012) DFT study of the water–gas shift reaction and coke formation on Ni(111) and Ni(211) surfaces. J Phys Chem C 116(38):20281–20291
57. Li J, Croiset E, Ricardez-Sandoval L (2012) Methane dissociation on Ni(100), Ni(111), and Ni(553): a comparative density functional theory study. J Mol Catal A Chem 365:103–114. doi:10.1016/j.molcata.2012.08.016
58. Blaylock DW, Zhu Y-A, Green WH (2011) Computational investigation of the thermochemistry and kinetics of steam methane reforming over a multi-faceted nickel catalyst. Top Catal 54(13–15):828–844
59. Bronsted JN (1928) Acid and basic catalysis. Chem Rev 5(3):231–338
60. Evans MG, Polanyi M (1938) Inertia and driving force of chemical reactions. Trans Faraday Soc 34:11–24
61. Wang S, Temel B, Shen J, Jones G, Grabow L, Studt F, Bligaard T, Abild-Pedersen F, Christensen C, Nørskov J (2011) Universal Brønsted-Evans-Polanyi relations for C–C, C–O, C–N, N–O, N–N, and O–O dissociation reactions. Catal Lett 141(3):370–373

62. Nørskov JK, Bligaard T, Logadottir A, Bahn S, Hansen LB, Bollinger M, Bengaard H, Hammer B, Sljivancanin Z, Mavrikakis M, Xu Y, Dahl S, Jacobsen CJH (2002) Universality in heterogeneous catalysis. J Catal 209(2):275–278
63. Studt F, Abild-Pedersen F, Bligaard T, Sørensen RZ, Christensen CH, Nørskov JK (2008) Identification of non-precious metal alloy catalysts for selective hydrogenation of acetylene. Science 320(5881):1320–1322
64. Asthagiri A, Janik MJ (2013) Computational catalysis. The Royal Society of Chem, Cambridge
65. Abild-Pedersen F, Lytken O, Engbæk J, Nielsen G, Chorkendorff I, Nørskov JK (2005) Methane activation on Ni(111): effects of poisons and step defects. Surf Sci 590(2–3):127–137
66. Miller SD, Kitchin JR (2009) Relating the coverage dependence of oxygen adsorption on Au and Pt fcc (111) surfaces through adsorbate-induced surface electronic structure effects. Surf Sci 603(5):794–801
67. Fischer F, Tropsch H (1926) The synthesis of petroleum at atmospheric pressures from gasification products of coal. Brennstoff Chem 7:97–104
68. Dry ME (2004) FT catalysts. Studies in surface science and catalysis. Elsevier, Amsterdam